Spring 5-2020

Estimating Bedrock Fracture Density of the Juneau Icefield, AK, to Inform Glacial Erosion Models

Colby Rand

ESTIMATING BEDROCK FRACTURE DENSITY OF THE JUNEAU ICEFIELD, AK, TO INFORM GLACIAL EROSION MODELS

by

Colby Rand

A Thesis Submitted to Partial Fulfillment
of the Requirements for a Degree of Honors
(Earth and Climate Sciences)

The Honors College

University of Maine

May 2020

Advisory Committee:

Seth Campbell, Assistant Professor in the School of Earth and Climate Sciences and Climate Change Institute, Advisor
Annie Boucher, Master's Student in the School of Earth and Climate Sciences
Peter Koons, Professor in the School of Earth and Climate Sciences and Climate Change Institute
Melissa Ladenheim, Associate Dean of the Honors College
Kristin Schild, Research Assistant Professor in the School of Earth and Climate Sciences and Climate Change Institute

ABSTRACT

Understanding glacial erosion rates is important because debris eroded by a glacier can impact glacier flow speeds, protect tidewater glaciers from rapid retreat, and impact the productivity of marine ecosystems. Traditionally, glacial erosion models rely on a rock's inherent "erodibility", typically presented as a constant, to predict how much debris will be eroded by the glacier. However, the erodibility of bedrock varies spatially as a function of its fracture density, fracture orientation, and lithology, so the notion of applying a constant erodibility term to a whole field site does not fully capture the actual bedrock dynamics of the system. In this work, I present a novel approach to quantify bedrock fracture density and orientation through the generation of a 3D Structure from Motion (SfM) model and the application of a series of machine learning algorithms. To test this approach, I quantified the fracture density of a glacial bedrock nunatak in the Juneau Icefield of Southeast (SE) Alaska. The spatial variation in fracture density across this nunatak was found to be highly variable. Bedrock in the SE region of this field site showed a relatively high fracture density (>20% fractured), whereas the central region of this field site showed a relatively low fracture density (0-10% fractured). Fracture orientations were shown to have a bimodal distribution, with the most common fracture orientations being approximately 0 and ± 90 degrees. This fracture density methodology and associated results can applied across the Juneau Icefield and other glacier systems to improve glacial bedrock erosion models.

ACKNOWLEDGMENTS

I am extremely grateful for all the people and organizations who helped fund and support this project. This work was made possible in part by the support of the Thomas E. Lynch Honors Thesis Scholarship. I wish to express my deepest gratitude to my advisor, Seth Campbell, for his guidance and for being a fantastic mentor for this project. I would also like to offer thanks to my committee members, Annie Boucher, Peter Koons, Melissa Ladenheim, and Kristin Schild, for their support and contributions. Additionally, I would like to thank Nicholas Whiteman for lending his photogrammetry knowledge and for his technical help. I would also like to thank Sam Roy for his guidance with the machine learning aspects of this project and for helping with the MATLAB programming. Furthermore, I would like to thank everyone involved at the Juneau Icefield Research Program for helping with the data collection and for being a source of inspiration. Finally, I would like to thank my family for their ongoing support during all of my endeavors.

TABLE OF CONTENTS

LIST OF FIGURES

LIST OF TABLES

CHAPTER I

INTRODUCTION

As glaciers flow from high to low elevations, they act like bulldozers, eroding the bedrock below them and picking up debris. The amount of debris eroded by a glacier is dependent on a number of factors, with basal sliding being the most crucial factor regulating glacial erosion (Näslund et al., 1997). Warm based (temperate) glaciers have water present at the bed because ice temperatures hover around 0° C. This basal water acts as a lubricant, allowing ice to slide over and erode the bedrock below it. Cold based (polar) glaciers, in contrast, remain at below freezing temperatures year-round and have no water present at the bed. In these glaciers, ice deforms around basal features primarily through non-erosive processes such as ice creep (Näslund et al., 1997).

Subglacial meltwater alone can be powerful enough to erode bedrock. Meltwater is believed to be responsible for the formation of crag and tail like features of various sizes (Shaw et al., 1987). These features form when meltwater flows over bedrock and encounters an obstacle of greater hardness, giving rise to differential erosion. A crescentic scour develops on the upstream side of the obstacle and extends downstream in the form of paired parallel furrows. These furrows become wider and shallower further downstream. The crescentic scour and corresponding furrows exhibit a smooth, polished nature, indicative of erosion by a fluid with low viscosity and high turbidity (Shaw et al., 1987). Small scale crag and tail features are known as rat tails and are only a few millimeters wide. Larger, intermediate scale features are known as sichelwannens and are commonly 1-2 m wide and 2-3 m long. Drumlins are even larger scale features with

widths up to 0.5 km and lengths in excess of 4-5 km. The formation of drumlins likely requires the presence of broad sheets of subglacial meltwater, but their formation is still under intense debate (Shaw et al., 1987).

The characteristics of the bedrock under a glacier influences how much erosion will occur. Rock types with a low hardness, such as sandstone, will erode much easier than rock with a higher hardness, such as granite. In addition, the size and density of cracks or joints in the bedrock is a major factor influencing rock strength. In general, subglacial erosion can be divided into two main processes: *abrasion*, or the grinding of fine-grained material, and *quarrying*, or the plucking of larger pieces of rock (Benn et al., 2014).

Abrasion wears down rock surfaces through the processes of striation and polishing. Striation occurs when rock particles lodged in the bottom of a glacier are dragged over the bed, gouging out thin grooves in the bedrock. Such striations provide clues to the direction of past ice flow because striations are oriented parallel to ice flow. Polishing is the smoothing of a rock surface through the removal of small protuberances. This process is analogous to sandpaper smoothing the surface of wood. Abrasion, however, is generally thought to account for less erosion than quarrying (Hooyer et al., 2012, Lane et al., 2015).

Quarrying is the fracture and removal of rock (> 1cm) from the bed surface. This occurs when the overburden pressure of ice laterally stresses fractured bedrock during flow. Fracturing and quarrying at the bed also occurs when melt water enters existing bedrock fractures, freezes, and expands, thereby applying stress to those fractures. This happens when a glacier flows over a bedrock obstacle, generating a high-pressure zone

on the stoss side of the obstacle and a low-pressure zone on the lee side of the obstacle. This high-pressure zone depresses the freezing point of the ice and transforms it into meltwater, which then flows around the obstacle to the low-pressure zone. This meltwater refreezes in the low-pressure zone because the freezing point of water here is increased. This melting and refreezing of water due to changing pressures is known as regelation (Iverson et al., 1995). As this meltwater refreezes and expands in bedrock fractures in the lee side of the obstacle, it increases stress on the rock and fractures it (Figure 1). This fracturing results in the detachment of rock fragments from the parent mass, which can then be entrained in the ice and transported downglacier (Bennett et al., 2009). High quantities of debris can be eroded through quarrying (Hooyer et al., 2012).

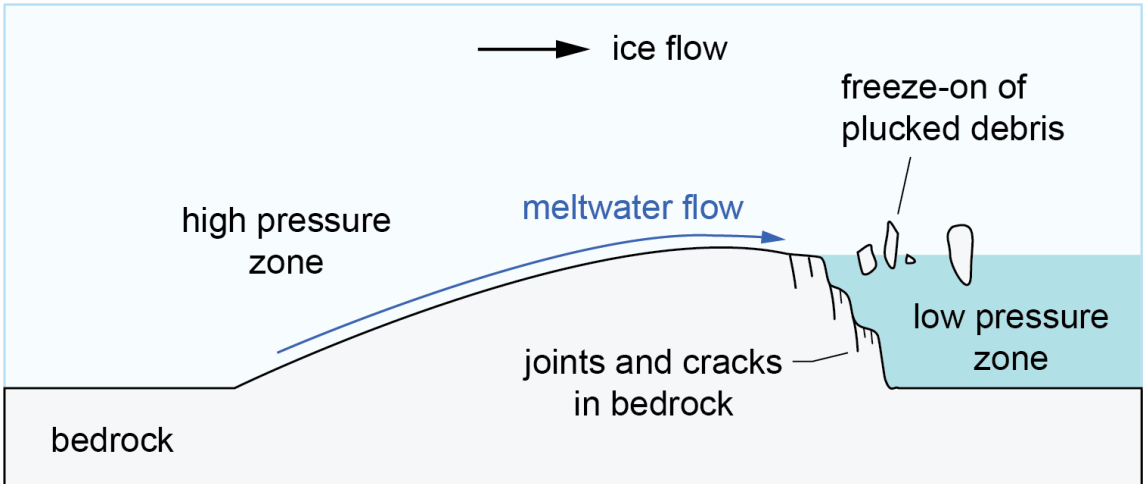

Figure 1. Quarrying of rock due to the regelation of ice around a bedrock obstacle. A high-pressure zone forms on the stoss side of the obstacle, melting the ice. This meltwater is transported around the obstacle where it refreezes on the lee side. Rock fragments are plucked from the lee side of the obstacle due to meltwater refreezing in joints and cracks in the bedrock. (illustration credit: Jacob Bendle)

The quantity of debris eroded by a glacier is largely governed by the strength of the rock below it (DiBiase et al., 2018; Dühnforth et al., 2010). Rock mass strength, or its

ability to resist erosion, is dependent on both the strength of intact rock and the density of fractures or cracks in the rock that reduce that strength (Clarke et al., 2011). The orientation of fractures is also important when determining bedrock strength because fractures oriented perpendicular to ice flow will experience more stress than fractures oriented parallel to ice flow (Lane et al., 2015). Therefore, bedrock with a high fracture density and a high proportion of fractures oriented perpendicular to ice flow should erode much more than the same type of bedrock with a low fracture density and a high proportion of fractures oriented parallel to ice flow. Field work conducted in the mountains of southern California supports this hypothesis (DiBiase et al., 2018; Dühnforth et al., 2010). These studies found that not only does fracture density control the amount of erosion that occurs, it can also modulate the dominant erosion process, namely quarrying vs. abrasion. Sites with a high fracture density (~1.8 m/m^2) showed evidence of high erosion rates (~0.2-1.0 mm/yr), with quarrying being the dominant erosion process. Conversely, sites with a low fracture density (~0.4 m/m^2) showed evidence of low erosion rates (~0.1-0.2 mm/yr), with abrasion being the dominant erosion process (DiBiase et al., 2018).

Debris eroded by glaciers becomes entrained within basal ice and is transported downglacier, with larger quarried material being broken up into smaller debris during transport. This debris acts as an agent of subglacial abrasion and has been shown to influence glacier dynamics. Glaciers that are underlain by unconsolidated sediments derived from erosion often experience faster ice velocities than glaciers underlain by solid bedrock because of deformation of the sediment layer. This deformation occurs because fine-grained, eroded sediments have a low cohesion and a high pore-water

pressure. Therefore, if the basal shear stress (gravitational driving stress) is greater than the yield strength of the sediment, deformation will occur and ice flow velocities will increase (Hart, 1995). Sediment deposited as a subaerial shoal at the terminus of a tidewater glacier can also act to protect it from rapid retreat, as seen at the Taku Glacier, Juneau Icefield (McNeil et al., 2020). This glacier began advancing in the late 19th century and actively calved into the Taku Inlet until 1950 when a subaerial shoal developed at its terminus. This shoal acted as a barrier to oceanographic influences and reduced calving on the glacier front, allowing it to continue its advance.

In the case of tidewater glaciers that terminate in the ocean, this debris is ultimately deposited just offshore via meltwater channels, or it is deposited further offshore after melting out of icebergs that calved off the glacier front. The fine-grained debris is believed to dynamically influence the productivity of offshore ecosystems. Subglacial meltwater discharge and its associated suspended sediments have shown to influence marine primary productivity inside fjords in Svalbard, Norway (Halbach et al., 2019). Here, high volumes of fine sediments derived from eroded sandstones and carbonate rocks limited light availability for phytoplankton. In contrast, coarser sediments eroded from gneissic and granitic bedrock were associated with more favorable light conditions, facilitating local phytoplankton blooms. In addition to modulating light availability, eroded sediments provide a source of nutrients for phytoplankton, depending on the source minerology. Erosion and chemical weathering can enrich glacial meltwater with phosphorus, nitrate, iron, silicic acid, and ammonium (Meire, 2016, O'Neel et al., 2015). These nutrients and micronutrients are necessary fertilizers for many phytoplankton, which are essential for the growth and productivity of

higher trophic levels. In coastal southeast Alaska, the productivity of phytoplankton influences the health of economically important fish species such as Pacific salmon (*Oncorhynchus* spp.) and herring (*Clupea pallasii*) (O'Neel et al., 2015).

Traditional glacial erosion models attempt to describe the evolution of glaciated mountain landforms by quantifying how much sediment is currently being eroded by glaciers, how much sediment was eroded in the past, and how much sediment could be eroded in the future (Herman et al., 2008). A common approach is to model glacial erosion as simply a function of the ice-sliding velocity μ_s at the ice-bedrock interface:

$$\frac{\delta z}{\delta t} = K_g |\mu_s|^{\,l}$$

where K_g ($m^{1-l}\,a^{l-1}$) is the glacial erosion constant and l is an arbitrary constant (Herman et al., 2008). However, the erodibility of bedrock varies spatially, and the notion of applying a constant glacial erosion term to a whole field site does not fully capture the actual dynamics accurately (DiBiase et al., 2018; Dühnforth et al., 2010). This spatial variation in erodibility can be calculated by measuring the bedrock's fracture density (Clarke et al., 2011). In this work, I calculate the fracture density of an exposed bedrock location within the Juneau Icefield (JIF), southeast Alaska. Since it is not possible to calculate fracture density directly under the JIF or other glaciers, I estimate fracture density of a nunatak adjacent to a glacier. This is done through the generation of a 3D Structure from Motion (photogrammetry) model derived from aerial drone footage and a combination of machine learning algorithms to discretize individual fractures and orientations. This fracture density information could potentially be used to better constrain glacial erosion models.

CHAPTER II

BACKGROUND

2.1 Geographic and Climatic Setting

The Juneau Icefield (JIF) is located in the northern Coast Mountains and crosses the border from southeast Alaska to British Columbia. At 3,830 km^2, the JIF is the fifth largest icefield in the Western Hemisphere (Melkonian et al., 2014). Icefield elevations range from sea level in the southwest, where the city of Juneau, Alaska is located, to ~2,500 m a.s.l. (Roth et al., 2018). Glaciers west of the Coast Range crest experience a maritime climate, with annual precipitation of around 3.0-4.0 m water equivalent (w.e.) and an average annual temperature at the equilibrium line altitude (ELA) of -1° C. Glaciers east of the crest receive substantially less precipitation (Pelto, 2013). This precipitation gradient is due to the orographic lifting of moisture-laden air parcels over the Coast Mountains, where they are forced to ascend and cool, resulting in the condensation of water vapor and precipitation west of the mountain divide. As air crosses over and descends on the eastern side of the divide, air parcels warm and cloud water evaporates, resulting in less precipitation (Ross et al., 2018). During the winter, the primary control on southeastern Alaskan climate is the Aleutian Low in the Gulf of Alaska (Fleming et al., 2000). This counterclockwise, circulating cyclone advects moisture from the ocean to southeast Alaska and promotes high levels of precipitation. During the summer, cyclone activity associated with the Aleutian Low weakens, and precipitation along southeast Alaska declines from its winter maximum.

The Camp-18 nunatak, located at 58° 50’ 05” N, 134° 16’ 33” W, is located near the United States – Canada border and has a mean elevation of 1690 m (Figure 2). This nunatak is home to Camp-18, a remote research base operated by the Juneau Icefield Research Program (JIRP). To the west, Camp-18 overlooks Gilkey Trench, a glacially carved valley where several glaciers converge. Vaughan-Lewis icefall to the south cascades approximately 515m down a steeply sloped bedrock valley into Gilkey Trench. The accumulation of ice at the bottom of the icefall results in the formation of ogives, or waves of ice (Hill, 2018). The convergence of the Vaughan-Lewis glacier, the Gilkey glacier, and other glaciers in the Gilkey Trench causes medial moraines to form between each individual glacier. During summer months, enough snow melts off the Camp-18 nunatak to expose the bedrock below.

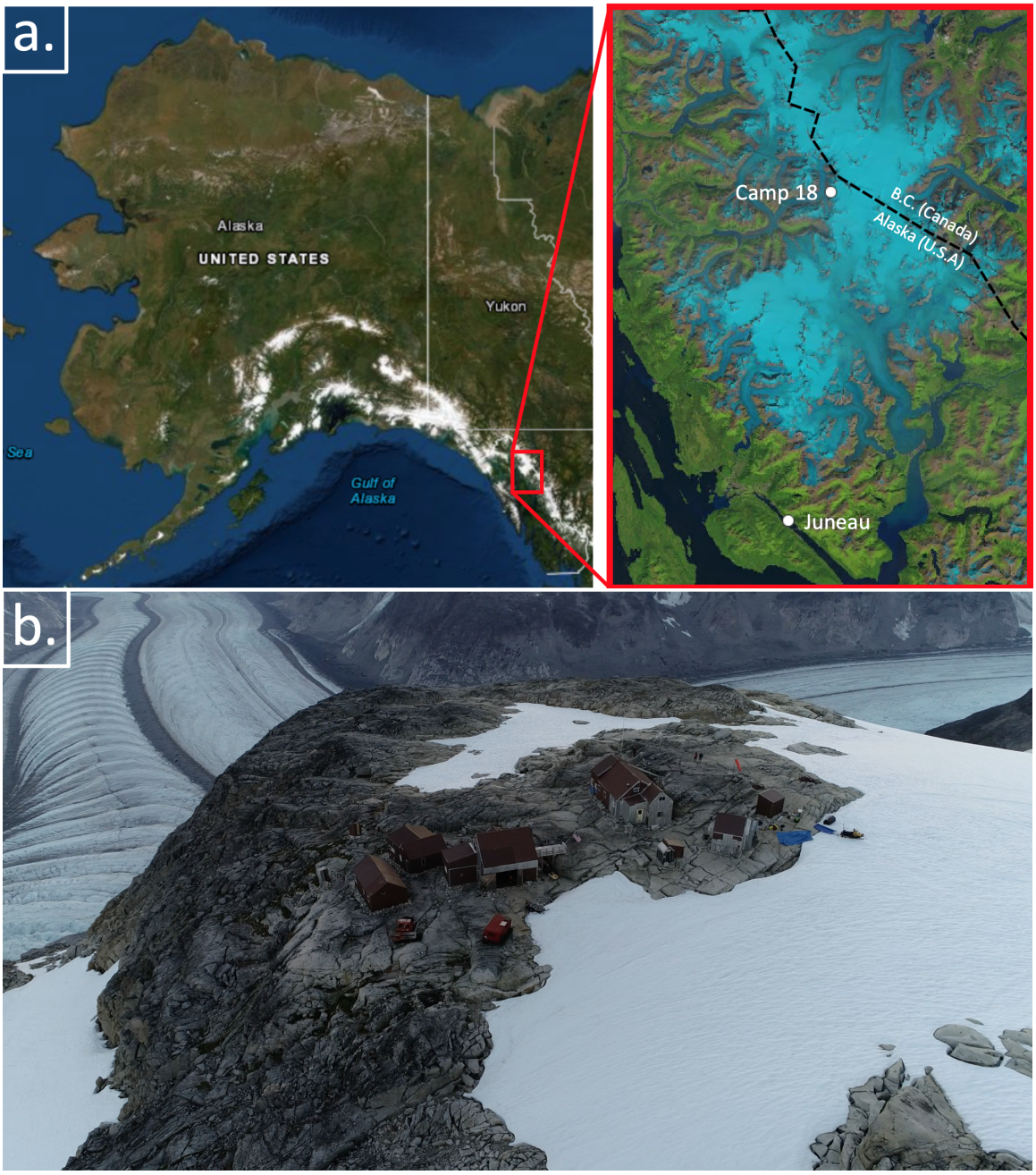

Figure 2. The Camp-18 nunatak, a remote research base for the Juneau Icefield Research Program (JIRP). **a.** The Juneau Icefield crosses the border from southeast Alaska to British Columbia. The Camp-18 nunatak is located just below the U.S. - Canada border and overlooks the Gilkey Trench. (USGS EarthExplorer) **b.** Aerial drone photograph of the Camp-18 nunatak with the Gilkey Trench in the background. This photo was taken in the summer of 2018, when the nunatak was only partially covered by snow. (photo credit: Seth Campbell)

2.2 Glaciologic Setting

Based on the Randolph Glacier Inventory (RGI; Pfeffer et al., 2014) the JIF is composed of 162 individual glaciers (Kienholz et al., 2015). Four of these glaciers have continuous mass-balance records exceeding 50 years. In particular, Taku and Lemon Creek glaciers have been measured since the mid 1940s and early 1950s, representing the longest mass balance records in North America and being among the longest records in the world (McNeil et al., 2020). Over the 1946-2018 period, all glaciers monitored, except one, have lost mass and retreated. The Taku glacier is the lone exception, having advanced and gained mass at an average rate of $+0.25 \pm 0.28$ m w.e. a^{-1} over this period. Since 2013, however, negative mass balance and glacier-wide thinning of Taku Glacier has prevailed. Because of this reversal, all glaciers in the Juneau Icefield are now believed to be in a state of mass loss (McNeil et al., 2020). Meltwater discharge from the Juneau Icefield, combined with the discharge from other icefields and glaciers in the Alaskan region, contribute the greatest quantity of meltwater to the world's oceans out of any mountain glacier region in the world (Figure 3). From 1961 to 2016, Alaskan glaciers have discharged 3,019 Gt of water, which is roughly one third of the 9,625 Gt of water discharged globally. This meltwater input from Alaska has resulted in approximately 8 mm in global sea level rise over the 1961 to 2016 period. The rate at which Alaskan glaciers have discharged meltwater has increased, with a mass-change rate of -0.6 m w.e. yr^{-1} (Zemp et al., 2019).

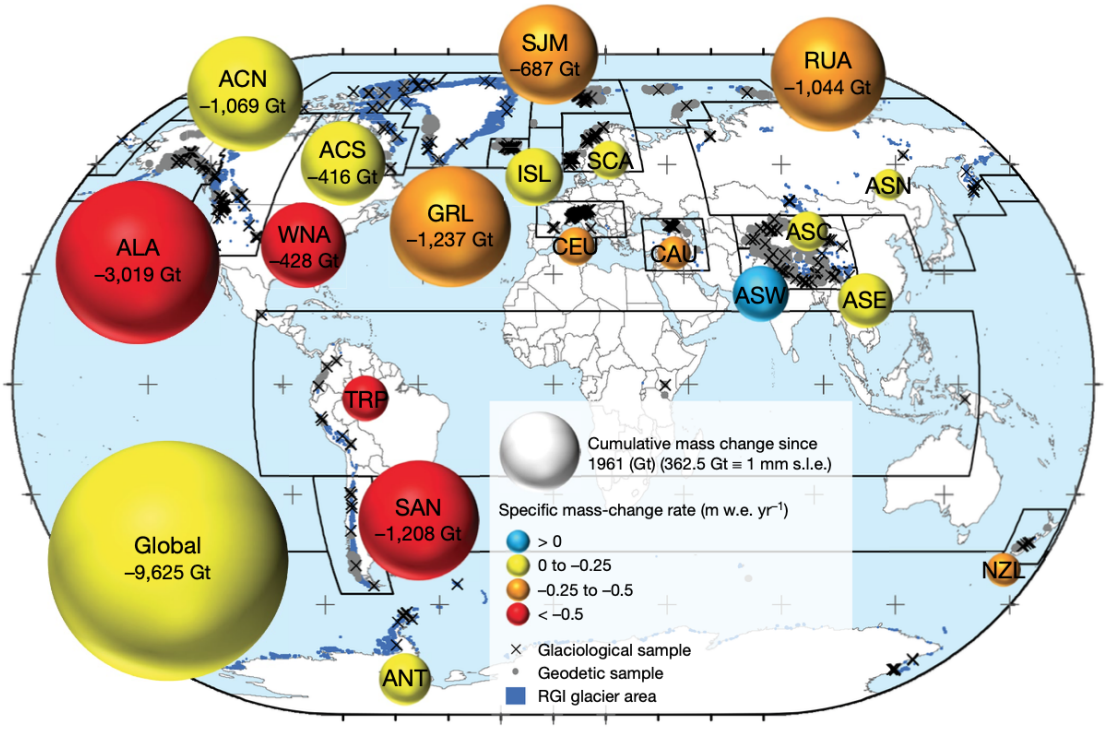

Figure 3. Regional mountain glacier meltwater discharge from 1961 to 2016. Cumulative and regional mass change is represented by the volume of the bubbles. Specific mass-change rates (m w.e. yr^{-1}) are indicated by the color of the bubbles. Alaskan glaciers (ALA) show the largest contribution to sea level rise, with a total discharge of -3,019 Gt, or about 8 mm sea-level equivalent (s.l.e.), and a mass-change rate of -0.6 m w.e. yr^{-1} (Zemp et al., 2019).

2.3 Geologic Setting

The bedrock geology of the Juneau Icefield is part of the Coast Mountains Complex (CMC), a 1760 km long coast-parallel volcanic arc system extending from northern Washington, through British Columbia and southeast Alaska, to southwestern Yukon (Barker et al., 1986). The CMC, also known as the Coast Plutonic Complex or the Coast Batholith, is believed to have developed in two stages between mid-Cretaceous and mid-Eocene time. The early stage (100-70 Ma) involved crustal thickening as the Wrangellia/Alexander terrane collided with the Stikine terrane, creating a linear, compressional structural zone that now marks the boundary between these two terranes (Crawford et al., 1987). The thickening at this collisional plate boundary resulted from tectonic stacking of crustal slabs, lubricated by the intrusion of melt at the base. The second stage (85-50 Ma) involved the intrusion of high-pressure granitic plutons and associated sills into the country rock (Crawford, 1987). These plutonic rocks make up the CMC, which can be divided into three main plutonic belts with NW-SE orientations: The Admiralty-Revillagigedo belt, the Great tonalite sill belt, and the easternmost Coast Mountains belt (Drinkwater, 1995). The Juneau Icefield is part of the Coast Mountains belt, which runs longitudinally along the United States-Canada border. The bedrock of this belt ranges from granite to tonalite in composition and exhibits moderate to high magnetic susceptibility. The predominant rock type is a massive, medium to coarse-grained, biotite-dominant, hornblende, and sphene bearing granodiorite (Brew, 1983). Radiometric ages vary, but potassium-argon and uranium-lead dating generally indicate the bedrock to be of mid-late Eocene origin (45-54 ma) (Brew, 1983; Barker, 1986). The Camp-18 nunatak primarily consists of these rock types (Figures 4 & 5).

Figure 4. Bedrock of the Camp-18 nunatak showing a steeply sloped section. Variable fracture densities are shown, with vegetation growing on some of the more highly fractured areas.

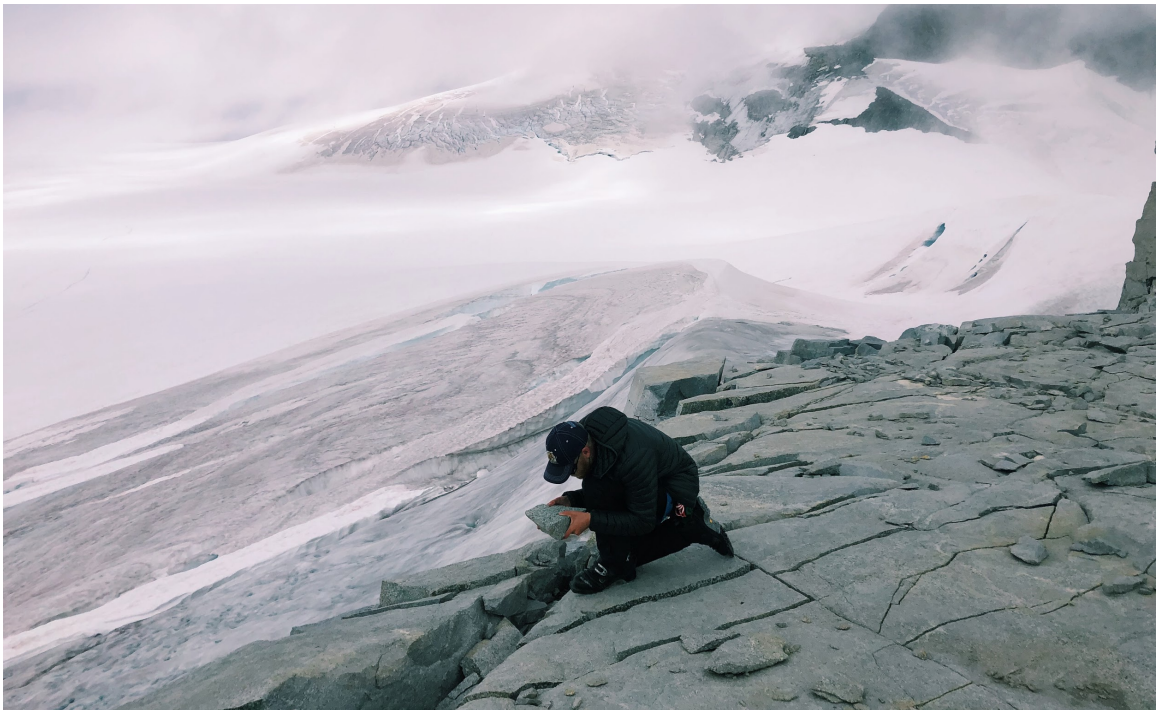

Figure 5. Photograph of me inspecting a rock on a nearby nunatak with the Llewellyn glacier in the background. Photo taken during an expedition to this nunatak to collect rocks for cosmogenic nuclide dating of the icefield (photo credit: Jocelyn Reahl).

CHAPTER III

METHODS

3.1 Data Acquisition

During the 2018 Juneau Icefield Research Program (JIRP) field season, drone video footage was collected of the Camp-18 nunatak. This footage was collected while the drone flow in a circular track above the nunatak, with the camera looking down at the ground surface. This footage was used to generate a 3D Structure from Motion (SfM) model of the nunatak using Agisoft Metashape software version 1.5.1. Previously acquired survey-grade GPS points (XY) at the corners of buildings on Camp-18 nunatak were used as ground control to properly georeference the model. The precise geographic position of each point was determined using a roving GPS coupled with a base station, whose GPS position and elevation was known precisely (sub-meter) by differential GPS. Unfortunately, the available GPS points of the buildings did not contain elevation (Z) information, so this was extracted from ArcticDEM, a 2 m resolution digital elevation model (DEM) of the Arctic using optical stereo imagery, high-performance computing, and open source photogrammetry software (Porter et al., 2018). These elevations were paired with each GPS point (Table 1).

Table 1. Geographic location of buildings at JIRP Camp-18. Latitude and longitude data were calculated with a handheld GPS unit paired with a differential GPS base station. Elevation data were extracted from ArcticDEM with 2 m resolution (Porter et al., 2018).

Label	Longitude	Latitude	Elevation (m)
Benstitute NE Corner	-134.2762181	58.83467105	1692
Benstitute NW Corner	-134.2763352	58.83464413	1691
Benstitute SE Corner	-134.2761776	58.83461954	1690
Benstitute SW Corner	-134.2762963	58.83459452	1689
Big Bird S Corner	-134.276529	58.83454077	1685
Capital NE Corner	-134.2760425	58.83461079	1691
Capital NW Corner	-134.2761884	58.83459185	1689
Capital SE Corner	-134.2760209	58.83456756	1690
Capital SW Corner	-134.2761662	58.83454861	1688
Cookshack NE Corner	-134.2761009	58.83494827	1699
Cookshack NW Corner	-134.2763566	58.83494162	1697
Cookshack SE Corner	-134.2760978	58.83491664	1698
Cookshack SW Corner	-134.2763506	58.83487961	1695
Gen Shed E Corner	-134.2759101	58.83499175	1699
Gen Shed N Corner	-134.2759808	58.83503489	1700
Gen Shed S Corner	-134.2759545	58.83496631	1699
Gen Shed W Corner	-134.2760167	58.83501426	1700
Joe's Loft E Corner	-134.2759961	58.83469917	1693
Joe's Loft NE Corner	-134.2760115	58.83476509	1695
Joe's Loft NW Corner	-134.2761766	58.8347503	1693
Joe's Loft S Corner	-134.2760451	58.83466065	1692
Joe's Loft SE Corner	-134.2760534	58.83469554	1693
Joe's Loft SW Corner	-134.2761106	58.83465652	1692
Joe's Loft W Corner	-134.2761713	58.83472809	1693
Ruby E Corner	-134.2762491	58.83450507	1685

3.2 Structure from Motion Model Generation

A Structure from Motion (SfM) model was generated from the drone video footage and known ground control points using Agisoft Metashape, a software product used for performing photogrammetric processing of digital images. This program allows for the generation of georeferenced dense point clouds, textured polygonal models, digital elevation models and orthomosaics from a set of overlapping images with the corresponding referencing information (Agisoft, 2020).

The first step involved extracting still frames from the drone video footage since the software only accepts images for processing. Metashape then automatically searched these still frames for feature points on overlapping images and matched these into tie points. This procedure resulted in the creation of a sparse point cloud model which represented the results of image alignment.

To georeference the model, ground control points (GCPs) were placed at each of the locations listed in Table 1. Ideally, GCPs should be evenly distributed within the area of interest, but the locations in Table 1 only covered the middle section of my field area, thus leading to greater uncertainty and lower resolution in the outer regions of the model. With these markers in place, a 3D mesh model was built from the sparse point cloud and GCPs. I checked the marker location on every photo in the 3D mesh model and refined its position to provide maximum accuracy. The marker coordinates in Table 1 were then imported into the model to specify the location of each GCP. Finally, a bounding box was used to define my study area and to exclude the outer parts of the model with a lower resolution.

A dense point cloud was generated from the 3D mesh model. For the following reconstruction parameters, quality was set to *high* and depth filtering was set to *aggressive*. Quality specifies the desired reconstruction quality, with high quality leading to more detailed and accurate geometry, but at the expense of longer processing. Depth filtering removed outliers among points due to noisy or badly focused images. Aggressive depth filtering is normally chosen for aerial data processing and was chosen here to remove noise from the scene.

A digital elevation model (DEM) of the Camp-18 nunatak was generated from the dense point cloud in Agisoft Metashape (Figure 6). This model displays the spatial variation in elevations across my entire study area. High elevations are displayed with warm colors and low elevations are displayed with cool colors. The buildings of Camp-18 are visible in the center of this model as anomalously high elevations.

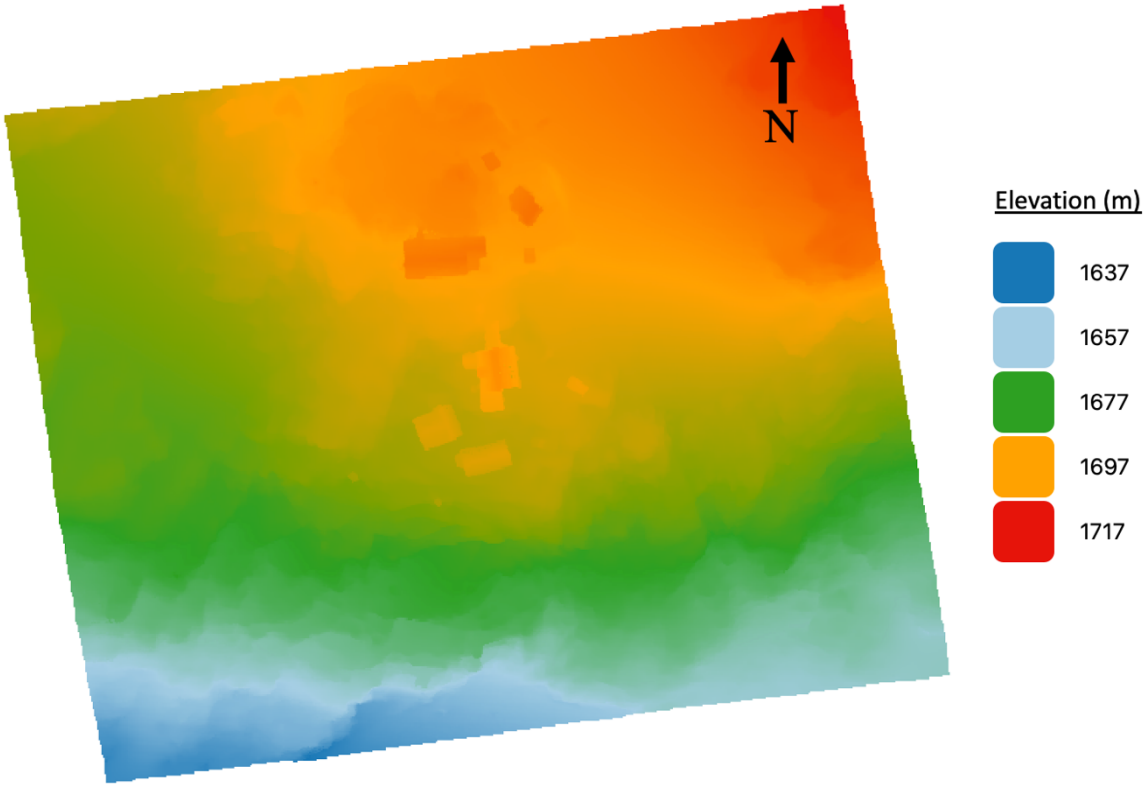

Figure 6. Digital elevation model (DEM) of the Camp-18 nunatak. The color scale of the model is matched with the elevation data on the right. Elevations range from high in the northeast to low in the southwest.

An orthomosaic model of the Camp-18 nunatak was also generated from the dense point cloud in Agisoft Metashape (Figure 7). This model is a detailed, accurate photo representation of my study area that has been created by stitching together the still frames captured by the drone. This map is geometrically corrected (orthorectified) such that the scale is uniform, and distances can be accurately measured across its surface. Due to the high density of ground control points at the buildings in the center of the study area and the lack of ground control points at the periphery of the study area, there is greater accuracy and resolution at the center of this map than there is at the outer limits.

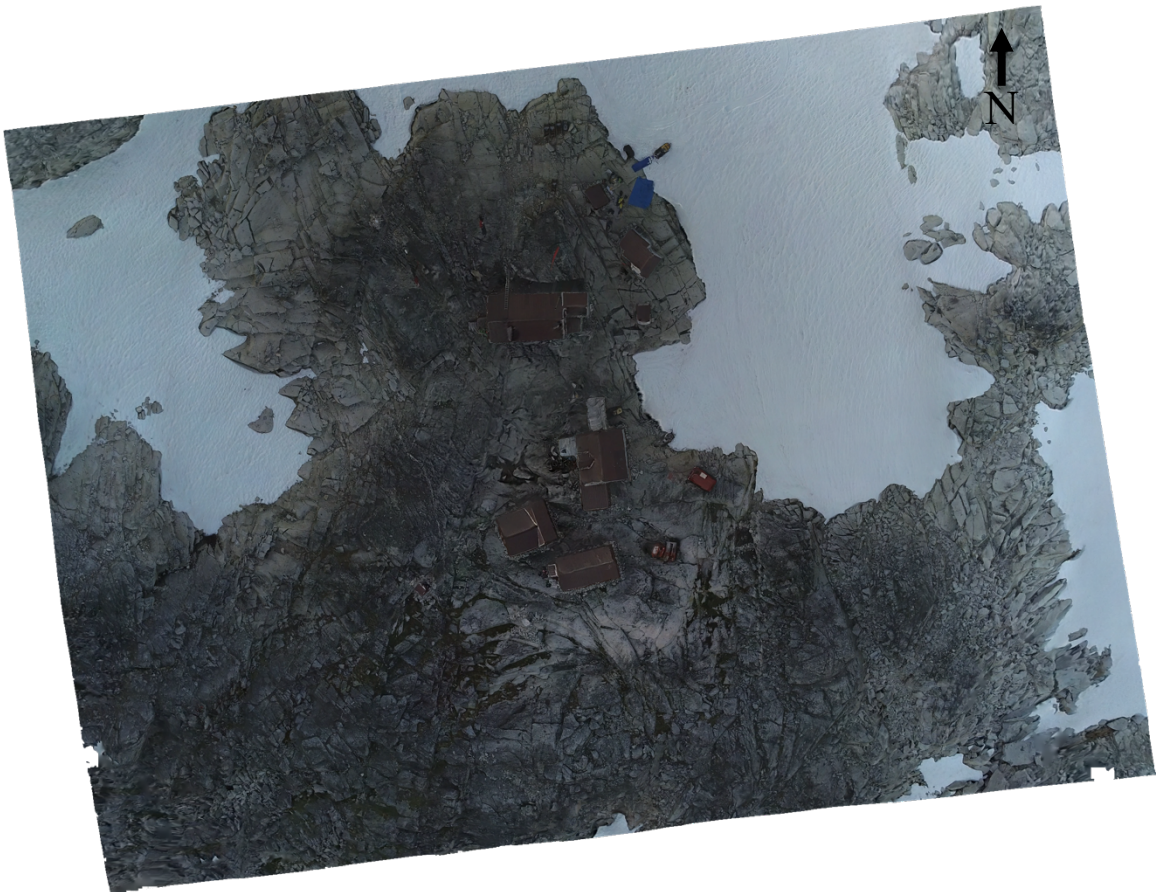

Figure 7. Orthomosaic model of the Camp-18 nunatak. Accuracy and resolution are higher in the center of the model than toward the periphery.

3.3 Machine Learning Algorithms

In order to discretize individual fractures of the Camp-18 nunatak, an edge detection algorithm was run on the orthomosaic generated from Agisoft Metashape. This algorithm was run in GIMP (GNU Image Manipulation Program), a free, open-source image editor. First, the orthomosaic is converted to grayscale, and then a Laplace edge detection algorithm is run on the grayscale image. This algorithm takes advantage of the relative color difference between fractures and the surrounding intact rock. Fractures often have shadows in them, so they appear darker than the surrounding rock. The

Laplace edge detection algorithm assigns regions of sharp color contrast as edges, which occurs where rock is fractured. The resulting image (Figure 8) symbolizes edges with white to light gray pixels and intact material with black to dark gray pixels.

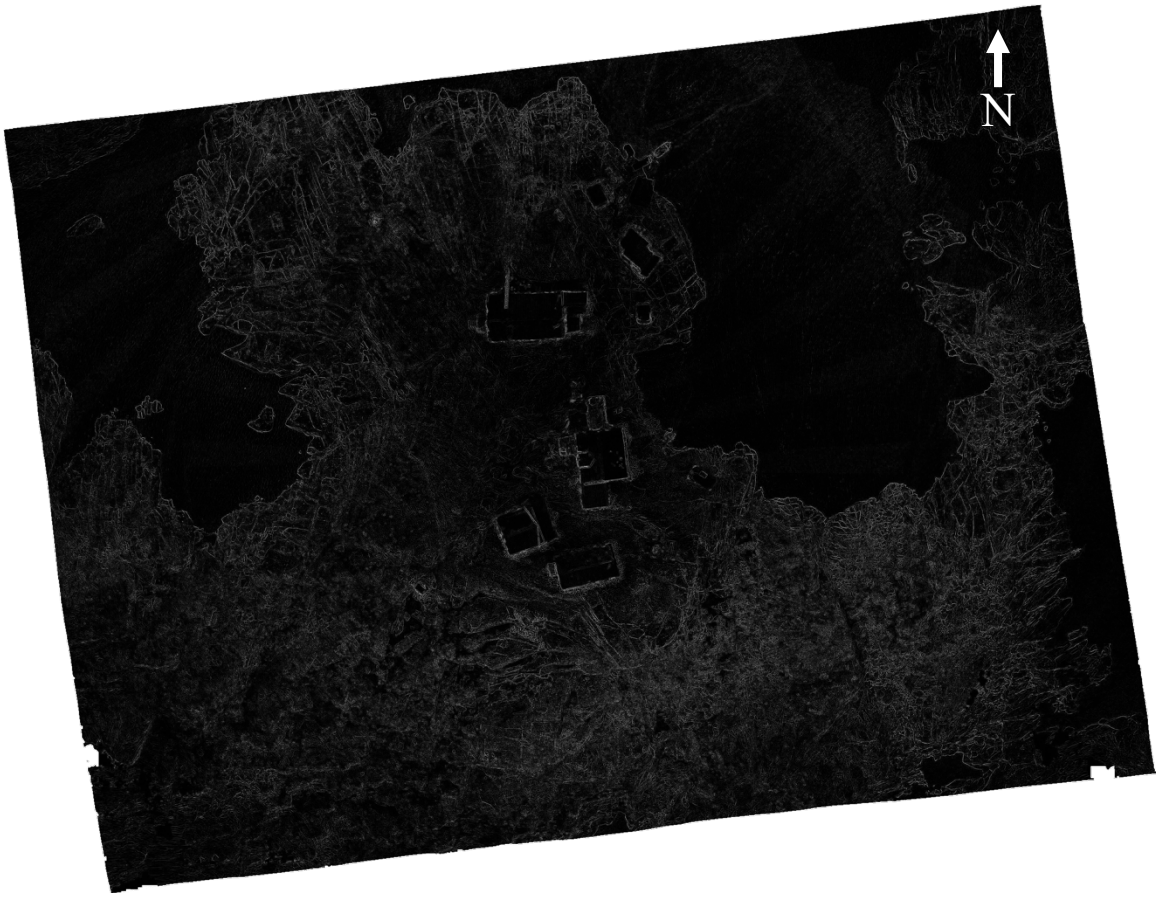

Figure 8. Laplace edge-detected image. This grayscale image shows the location of edges with white to light gray pixels and intact material with black to dark gray pixels.

While Figure 8 does well at representing fractures as edges, non-fracture features, such as dark or wet rocks, vegetation, or small debris, are also identified as edges by this algorithm. To refine Figure 8 and reduce the amount of non-fracture features identified, a series of algorithms were run in MATLAB. The first step involved converting the grayscale image to a binary image. The original grayscale image is composed of pixels

that have an intensity value between 0 (black) and 255 (white). A histogram showing the distribution of intensity values among pixels is shown in Figure 9. Since most of the pixels have an intensity close to 0 and few have an intensity close to 255, I created a binary image with all pixels below a threshold value of 38 as black and all pixels above a threshold value of 38 as white. The resulting binary image is shown in Figure 10.

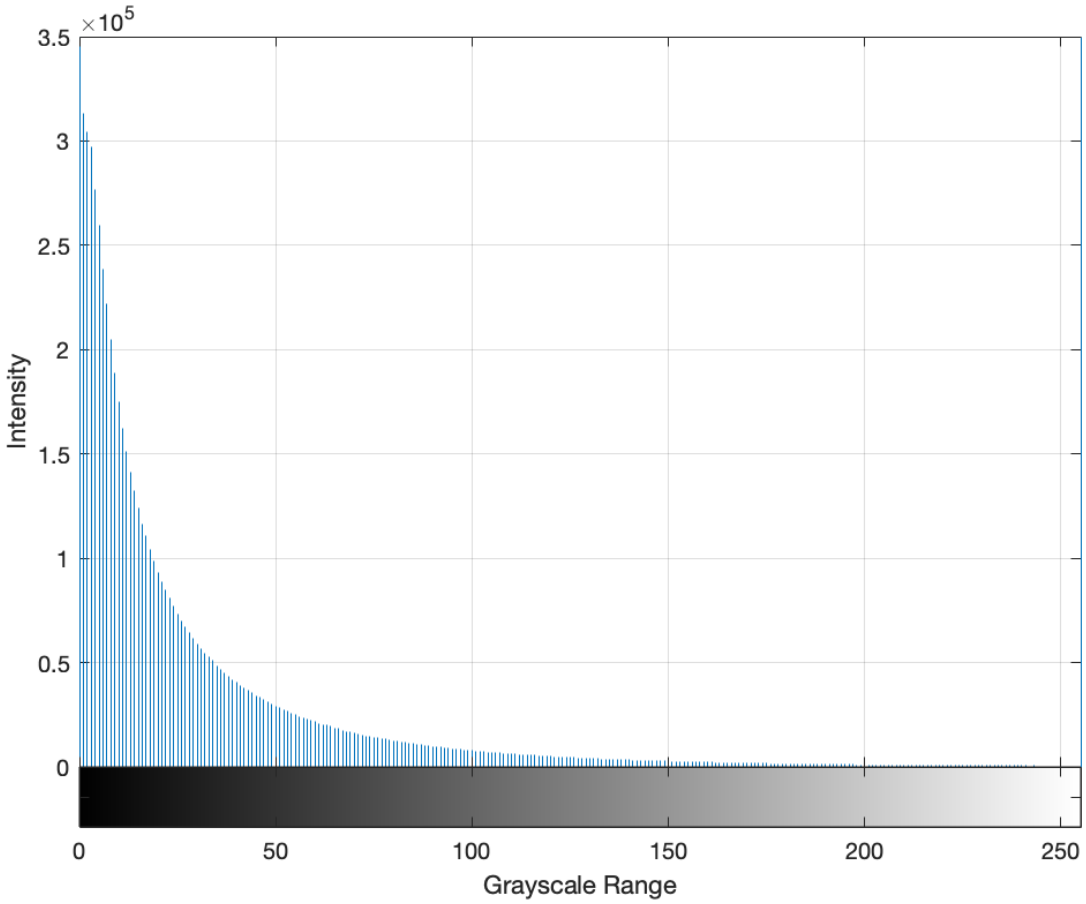

Figure 9. Histogram of grayscale intensities of pixels in the Laplace edge-detected image. All pixels have values that range from 0 to 255, which correspond to black and white respectively.

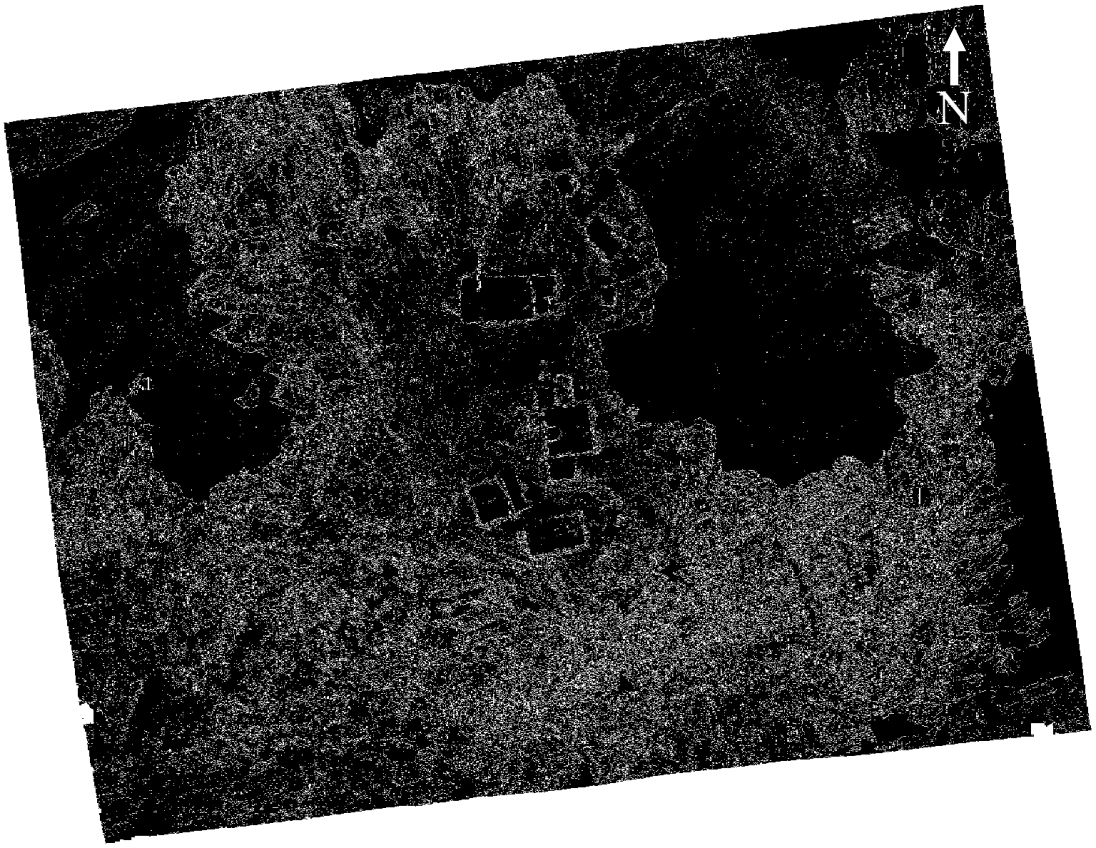

Figure 10. Binary Laplace edge-detected image. This binary image shows the location of edges with white pixels and intact material with black pixels.

For every white pixel in this image that has at least one adjacent white pixel, this group of pixels is considered to be a "connected component". Bedrock fractures will have many white pixels next to each other since these fractures can be meters long, and thus will have a connected component composed of many pixels. Single isolated pixels or small groups of pixels making up a connected component often represent noise that is not a real fracture. Figure 10 displays a significant amount of noise associated with non-fracture features. To reduce this noise, I removed all connected components from the binary image 10 pixels in size or smaller. Various threshold values were tested but a number lower than 10 would remove too little noise, whereas a number greater than 10

would remove a greater amount of real fracture data in addition to noise. The refined image is shown in Figure 11.

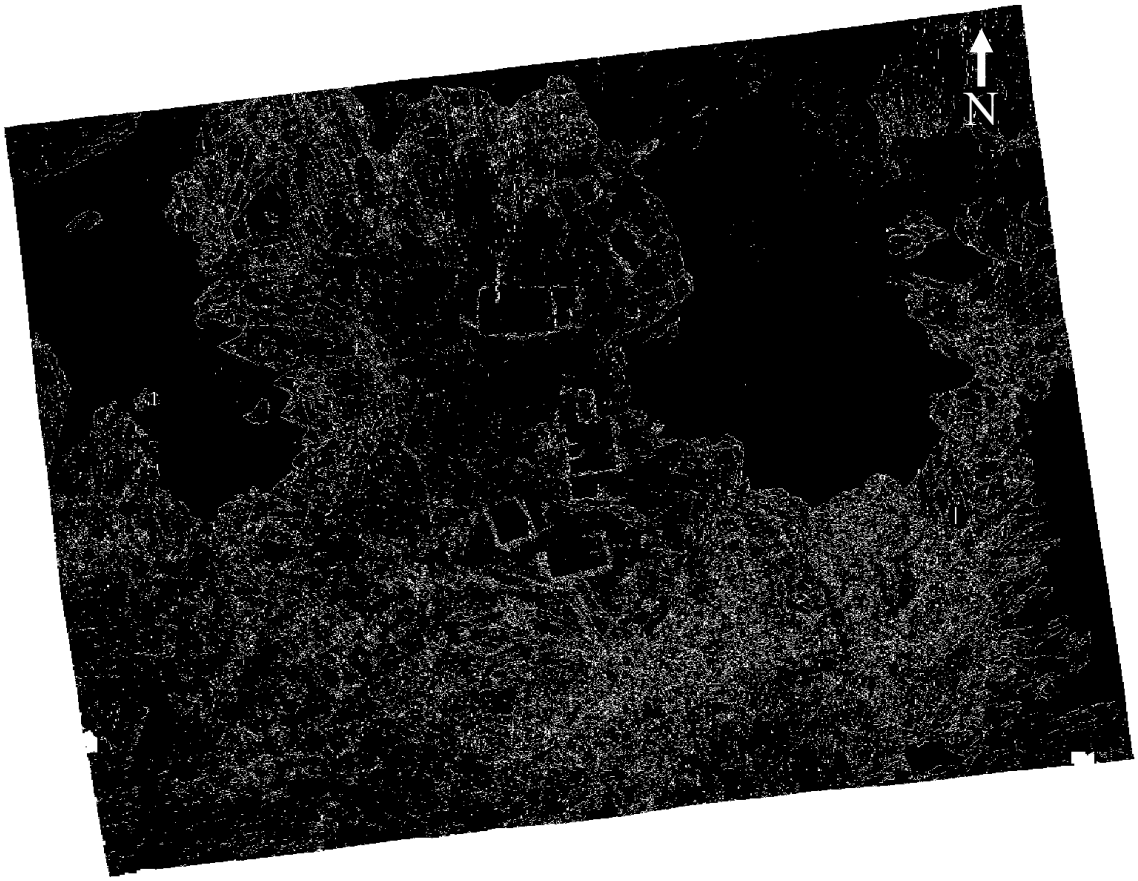

Figure 11. Refined binary Laplace edge-detected image. Connected components composed of groups of 10 pixels or smaller were removed from this figure to reduce the noise associated with non-fracture features.

In order to quantify the spatial variation in fracture density across the Camp-18 nunatak, I divided Figure 11 into an array of 2 m x 2 m (4 m^2) cells. Within each cell, I calculated the number of white and black pixels present. By dividing the number of white pixels by the total number of pixels, I quantified the surface area percentage of each 4 m^2 cell that is fractured. Figure 12 shows the spatial variation in fracture density across the Camp-18 nunatak. Warm colors indicate a high percentage of rock is fractured and cool

colors indicate either a low percentage of rock is fractured, or the bedrock is covered with snow, thus obscuring the fractures.

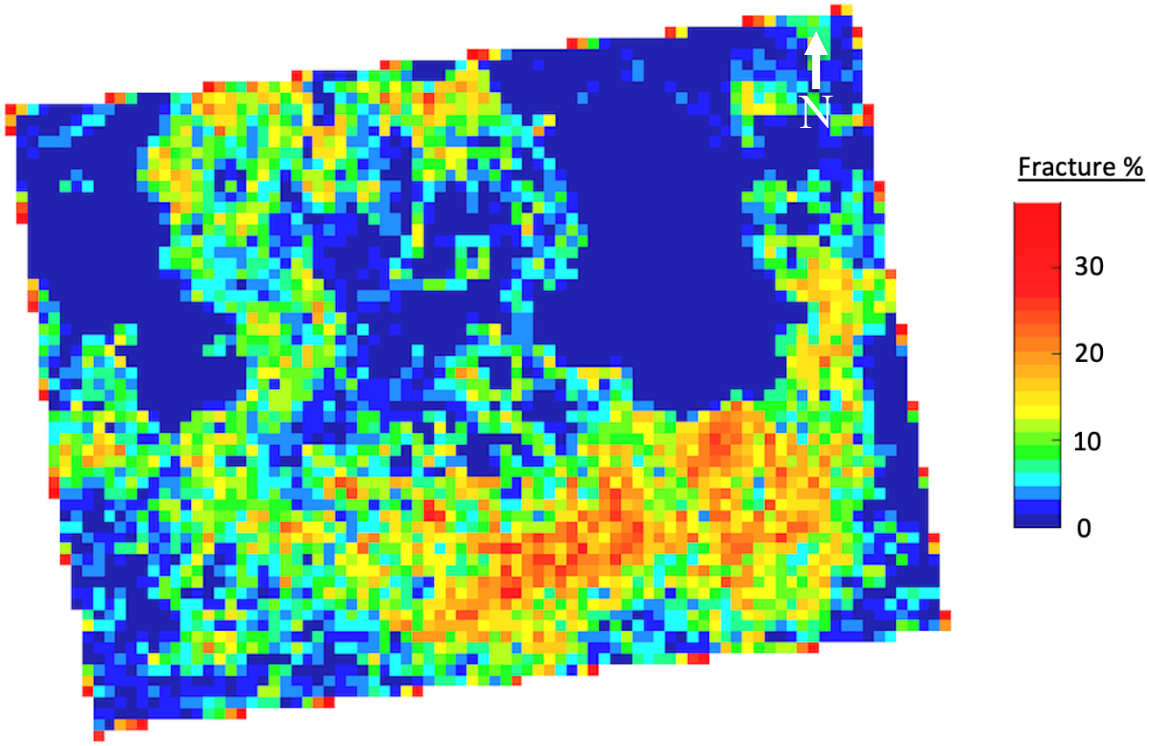

Figure 12. Spatial variation in fracture density across the Camp-18 nunatak. Color scale corresponds to the surface area percentage of each 4 m^2 cell that is fractured.

Each connected component also contains orientation data that represents the average orientation for its associated group of pixels. This orientation is calculated as the angle between the x-axis and the major axis of the ellipse encircling the connected component. Orientation values range from -90 to 90 degrees. I calculated the average orientation for each connected component in the Laplace edge-detected image and graphed this on a histogram (Figure 13). This histogram represents the range of fracture orientations across the Camp-18 nunatak. Note, I tested the uncertainties in fracture orientation in response to the removal of various connected component threshold values by developing histograms for multiple levels of filtering above and below 10 pixels.

Results showed little variability in fracture orientation, suggesting that the filtering did not negatively impact the orientation information.

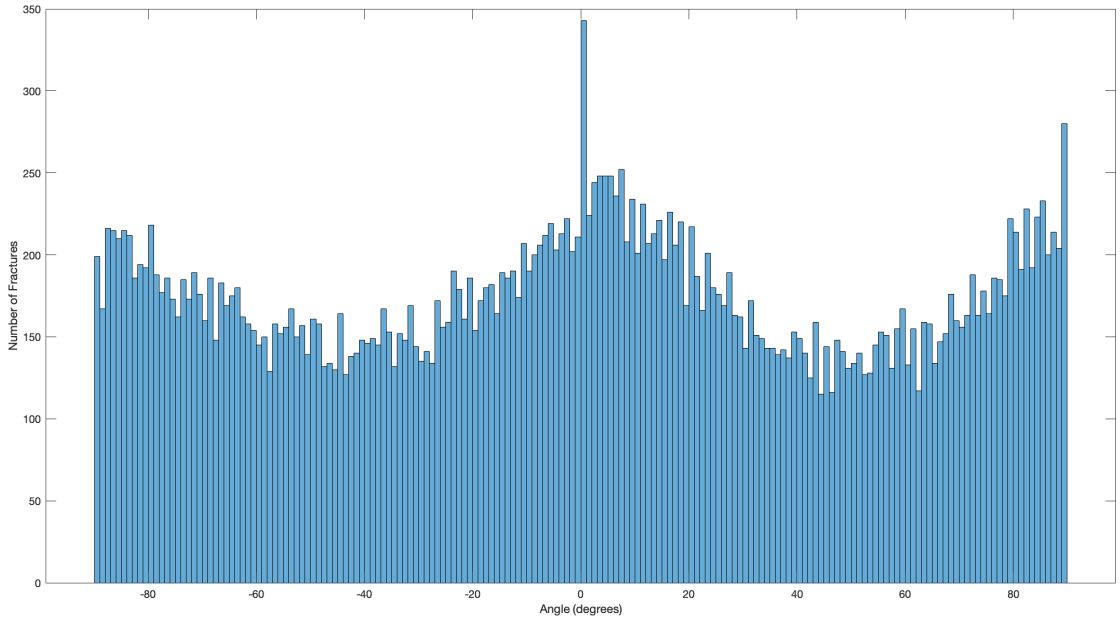

Figure 13. Histogram displaying the range of fracture orientations across the Camp-18 nunatak. Fracture orientations are defined as the angle between the x-axis and the major axis of an ellipse encircling a connected component.

CHAPTER IV

RESULTS

The spatial variation in fracture density across the Camp-18 nunatak is highly variable. Figure 12 shows a relatively high fracture density (>20%) in the southeastern region of my study area compared to a relatively low fracture density (0-10%) in the central region of my study area. This central region contains many buildings which obscure the fractures below them. The edges of the buildings show up as fractures in the binary image, but the roofs show up as dark regions with few fractures. Buildings create an artificial signal in the fracture density figures and must therefore be considered when analyzing bedrock regions that contain numerous man-made structures. Large contiguous regions of 0% fracture density occur where bedrock is covered by snow, thus also obscuring all fractures below it. The high fracture density pixels surrounding the edges of this image are artifacts of the image processing, and do not represent real fracture density percentages.

I interpret regions with a high fracture density to represent low rock mass strength, which would be more prone to subglacial erosion via quarrying. I interpret regions with a low fracture density to represent higher rock mass strength, which would be more resistant to subglacial erosion, with abrasion being the dominant erosion type (Clarke et al., 2011; DiBiase et al., 2018). Since it is not possible to measure rock mass strength directly underneath a glacier, the average fracture density percentage of an adjacent nunatak is measured to give an approximation of the rock mass strength under the glacier. In this case, the average fracture density of the Camp-18 nunatak gives an

approximation of the rock mass strength of bedrock underlying the Vaughn Lewis Icefall to the south of this nunatak. Glacial erosion models which seek to quantify the amount of debris eroded by the Vaughn Lewis glacier could be improved by using local fracture density estimations such as this, as opposed to using a constant erodibility term for the whole glacier.

In addition to fracture density, fracture orientations are also shown to vary spatially across the Camp-18 nunatak, as shown in Figure 13. This histogram reveals a bimodal distribution of fracture orientations, with the most common orientations being approximately 0 and ± 90 degrees. This makes sense considering the source granodiorite contains many fractures oriented perpendicular to one another. If the majority of these fractures are oriented perpendicular to past dominant ice flow, then increased quantities of debris would have been eroded from the bedrock. Likewise, if the majority of these fractures were oriented parallel to past dominant ice flow, then lower quantities of debris would have been eroded from the bedrock. If paleo-ice flow directions are known, then this fracture orientation information may be used to further constrain glacial erosion models (Lane et al., 2015).

CHAPTER V

CONCLUSIONS / FUTURE WORK

I present a novel approach to quantifying bedrock fracture density in order to improve glacial erosion models. While this approach was used here to quantify bedrock fracture density for part of the Camp-18 nunatak, the same workflow could theoretically be replicated on any other bedrock surface. Replicating this process for all nunataks and surrounding bedrock of the Juneau Icefield would lead to a much better understanding of the spatial variation in bedrock fracture density and dominant fracture orientations across the whole icefield. This would lead to new, improved constraints for glacial erosion models in the region.

In the development of this process, much was learned in how to improve this workflow and make these calculations quicker and more accurate. The original drone video footage I used to construct the Structure from Motion (SfM) model did not contain GPS metadata, so I was unable to use the camera location to georeference the SfM model. In the future, photographs should be shot with the drone instead of recording video, because unlike video footage, still images contain precise location information. Additionally, since I did not anticipate the video footage to be missing location metadata, I was forced to rely solely upon the GPS positions of the JIRP Camp-18 buildings to serve as GCPs. However, since these GCPs were all located toward the center of my SfM model, the outer limits of this model did not contain the same resolution and accuracy as the interior. Therefore, if GCPs are continued to be used in the future, they should be placed throughout the study area, and not just toward the interior. This will refine the

resolution and accuracy throughout the model. Furthermore, the GPS locations of the Camp-18 buildings did not contain elevation data, so I relied upon ArcticDEM for this information, which came with the limitation of 2 m resolution. In the future, precise elevation data should be collected alongside latitude and longitude when recording the geographic location of GCPs.

To compliment the fracture orientation information, I would like to derive historical ice flow directions from erosive features in the bedrock such as striations and chatter marks. Mapping these features can reveal historical ice flow direction because striations are oriented parallel to past ice flow and chatter marks point in the direction of past ice flow. Comparing the direction of historical ice flow to the local fracture orientations, in addition to the local fracture density, could imply roughly how much debris was eroded during glaciation.

REFERENCES

Agisoft. (2020). *Agisoft Metashape User Manual, Standard Edition, Version 1.6*. Retrieved from: https://www.agisoft.com/pdf/metashape_1_6_en.pdf

Barker, F., Arth, J. G., Stern, T. W. (1986). Evolution of the Coast batholith along the Skagway traverse, Alaska and British Columbia. *American Mineralogist*, *71*(3-4), 632-643.

Benn, D., & Evans, D. J. (2014). Glaciers and glaciation. *Routledge*, 259-267.

Bennett, M.R., and Glasser, N.F. (2009) Glacial Geology: Ice Sheets and Landforms. *Wiley-Blackwell,* 109-131.

Brew, D. A., Morrell, R. P. (1983). Intrusive rocks and plutonic belts of southeastern Alaska, USA. *Circum-Pacific plutonic terranes: Geological Society of America Memoir*, *159*, 171-193.

Clarke, B. A., & Burbank, D. W. (2011). Quantifying bedrock-fracture patterns within the shallow subsurface: Implications for rock mass strength, bedrock landslides, and erodibility. *Journal of Geophysical Research: Earth Surface*, *116*(F4).

Crawford, M. L., Hollister, L. S., Woodsworth, G. J. (1987). Crustal deformation and regional metamorphism across a terrane boundary, Coast Plutonic Complex, British Columbia. *Tectonics*, *6*(3), 343-361.

DiBiase, R. A., Rossi, M. W., & Neely, A. B. (2018). Fracture density and grain size controls on the relief structure of bedrock landscapes. *Geology*, 46(5), 399–402.

Drinkwater, J. L., Ford, A. B., Brew, D. A. (1995). Geology, petrography, and geochemistry of granitic rocks from the Coast Mountains Complex near Juneau, southeastern Alaska (No. 95-638). *US Geological Survey*.

Dühnforth, M., Anderson, R. S., Ward, D., & Stock, G. M. (2010). Bedrock fracture control of glacial erosion processes and rates. *Geology*, 38(5), 423–426.

Fleming, M. D., Chapin III, F. S., Cramer, W., Hufford, G. L., & Serreze, M. C. (2000). Geographic patterns and dynamics of Alaskan climate interpolated from a sparse station record. *Global Change Biology*, *6*(S1), 49-58.

Halbach, L., Assmy, P., Vihtakari, M., Hop, H., Duarte, P., Wold, A., ... & Wulff, A. (2019). Tidewater glaciers and bedrock characteristics control the phytoplankton growth environment in an Arctic fjord. *Frontiers in Marine Science*, 6, 254.

Hart, J. K. (1995). Subglacial erosion, deposition and deformation associated with deformable beds. *Progress in Physical Geography*, 19(2), 173-191.

Herman, F., Braun, J. (2008). Evolution of the glacial landscape of the Southern Alps of New Zealand: Insights from a glacial erosion model. *Journal of Geophysical Research: Earth Surface*, 113(F2).

Hill, Ann. (2018). Evolution of ogives on Gilkey Glacier, Alaska. *Geosciences Honors Theses*. https://creativematter.skidmore.edu/geosci_stu_schol/1

Hooyer, T. S., Cohen, D., & Iverson, N. R. (2012). Control of glacial quarrying by bedrock joints. *Geomorphology*, *153*, 91-101.

Iverson, N. R., & Semmens, D. J. (1995). Intrusion of ice into porous media by regelation: A mechanism of sediment entrainment by glaciers. *Journal of Geophysical Research: Solid Earth*, *100*(B6), 10219-10230.

Kienholz, C., Herreid, S., Rich, J. L., Arendt, A. A., Hock, R., & Burgess, E. W. (2015). Derivation and analysis of a complete modern-date glacier inventory for Alaska and northwest Canada. *Journal of Glaciology*, *61*(227), 403-420.

Lane, T. P., Roberts, D. H., Rea, B. R., Cofaigh, C. Ó., & Vieli, A. (2015). Controls on bedrock bedform development beneath the Uummannaq Ice Stream onset zone, West Greenland. *Geomorphology*, *231*, 301-313.

Meire, L., Meire, P., Struyf, E., Krawczyk, D. W., Arendt, K. E., Yde, J. C., ... & Meysman, F. J. R. (2016). High export of dissolved silica from the Greenland Ice Sheet. *Geophysical Research Letters*, 43(17), 9173-9182.

Melkonian, A. K., Willis, M. J., & Pritchard, M. E. (2014). Satellite-derived volume loss rates and glacier speeds for the Juneau Icefield, Alaska. *Journal of Glaciology*, *60*(222), 743-760.

Näslund, J. O. (1997). Subglacial preservation of valley morphology at Amundsenisen, western Dronning Maud Land, Antarctica. *Earth Surface Processes and Landforms: The Journal of the British Geomorphological Group*, 22(5), 441-455.

O'Neel, S., Hood, E., Bidlack, A. L., Fleming, S. W., Arimitsu, M. L., Arendt, A., ... & Hayward, G. D. (2015). Icefield-to-ocean linkages across the northern Pacific coastal temperate rainforest ecosystem. *BioScience*, *65*(5), 499-512.

Pelto, M., Kavanaugh, J., & McNeil, C. (2013). Juneau Icefield Mass Balance Program 1946-2011. *Earth System Science Data*, 5(2).

Pfeffer, W. T., Arendt, A. A., Bliss, A., Bolch, T., Cogley, J. G., Gardner, A. S., ... & Miles, E. S. (2014). The Randolph Glacier Inventory: a globally complete inventory of glaciers. *Journal of Glaciology*, *60*(221), 537-552.

Porter, C., Morin, P., Howat, I., Noh, M., Bates, B., … & Bojesen, M. (2018). ArcticDEM. *Harvard Dataverse, V1.* https://doi.org/10.7910/DVN/OHHUKH

Roth, A., Hock, R., Schuler, T. V., Bieniek, P. A., Pelto, M., & Aschwanden, A. (2018). Modeling winter precipitation over the Juneau Icefield, Alaska, using a linear model of orographic precipitation. *Frontiers in Earth Science*, *6*, 20.

Shaw, J., & Sharpe, D. R. (1987). Drumlin formation by subglacial meltwater erosion. *Canadian Journal of Earth Sciences*, *24*(11), 2316-2322.

Zemp, M., Huss, M., Thibert, E., Eckert, N., McNabb, R., Huber, J., ... & Thomson, L. (2019). Global glacier mass changes and their contributions to sea-level rise from 1961 to 2016. *Nature*, *568*(7752), 382-386.

AUTHOR'S BIOGRAPHY

Colby Rand was born in Bangor, Maine on June 30, 1997. He was raised in Orrington, ME and graduated from Brewer High School in 2015. Colby completed his undergraduate degree in Earth Sciences with a concentration in Climate Sciences at the University of Maine. He studied abroad at the University of Aberdeen in Scotland and attended field camp in Alaska as a participant on the Juneau Icefield Research Program. He is a member of the Sigma Phi Epsilon (SigEp) fraternity and the UMaine Geology Club. After graduation, Colby will work as a Water Resources GIS Intern at the New Hampshire Department of Environmental Services, and in the future, he plans to attend graduate school to study glaciology.